Networking Assessment of ROADM Architecture based on Photonics Integrated WSS for 800G Multi-band Optical Transport

JOURNAL OF
Optical Communications
and Networking

Networking assessment of ROADM architecture based on a photonics integrated WSS for 800G multi-band optical transport

Muhammad Umar Masood,[1,*] Lorenzo Tunesi,[1] Ihtesham Khan,[1] Bruno Correia,[1] Rasoul Sadeghi,[1] Enrico Ghillino,[2] Paolo Bardella,[1] Andrea Carena,[1] and Vittorio Curri[1]

[1]DET, Politecnico di Torino, Corso Duca degli Abruzzi, 24, 10129, Torino, Italy
[2]Synopsys, Inc., 400 Executive Boulevard, Suite 101, Ossining, New York 10562, USA
*muhammad.masood@polito.it

Received 17 March 2023; revised 24 June 2023; accepted 24 June 2023; published 12 September 2023

The capacity of the optical transport network must be expanded to support the increasing demand due to bandwidth-intensive applications. Multi-band transmission solutions can achieve this goal by exploiting the low-loss optical spectrum windows while maintaining the same existing fiber infrastructure, increasing the network's capacity, and minimizing the operator capital expenditure (CAPEX) by limiting the need for a new fiber deployment. In the context of multi-band transmission, this work proposes a novel reconfigurable optical add–drop multiplexer (ROADM) architecture using a modular photonic integrated multi-band wavelength selective switch (WSS) that operates over multi-bands (S + C + L). This study focuses on conducting a comprehensive network performance analysis of different settings, enabling operation from 400G up to 800G using the proposed multi-band WSS on two real network topologies: German and Italian. The results provide the potential benefits of transitioning from traditional C-band transmission to multi-band transmission based on overall network performance.

https://doi.org/10.1364/JOCN.489754

1. INTRODUCTION

It is estimated that global Internet traffic is projected to grow at a compound annual growth rate (CAGR) of 30% [1]. The introduction of 5G technology is expected to increase wireless network capacity substantially; to support this increase, all other network segments will require optical transmission over fiber infrastructures. To meet this growing demand, network operators must develop cost-effective, scalable, and flexible strategies to increase the capacity of their existing infrastructure. These efforts are essential to ensure the reliable and efficient operation of the Internet in the future. The current state-of-the-art wavelength division multiplexing (WDM) optical infrastructure takes advantage of the C-band, which has a bandwidth of 4.8 THz, as a transmitting window from long-haul/submarine to urban networks. By employing a preferred polarization multiplexed rectangular 16-ary quadrature amplitude modulation (PM-16QAM) scheme, this technique allows data transfer rates of around 30 Tbps per fiber. It is important to consider that the installation of new fiber to increase capacity can result in high costs, particularly in situations where fiber resources are limited [2]. Within this context, multi-band transmission, defined as transmitting data through a broader range of low-loss optical fiber spectral bandwidths, presents a favorable solution to improve network capacity and effectively repurpose existing fiber infrastructure.

However, the incorporation of components outside of the C-band spectrum can increase network costs, especially amplifiers that are potentially expensive, but this can minimize the need for a new fiber infrastructure. Moreover, stimulated Raman scattering (SRS) can lead to degradation and imbalanced transmission quality across multiple bands, negatively impacting network capacity, particularly on larger networks. Hence, conducting a thorough analysis of the advantages of incorporating multi-band network components in a multi-band transmission system versus single-band transmission is decisive to evaluate the overall performance of the network.

In this framework, there are two possible approaches to increase the capacity of the optical network infrastructure: spatial division multiplexing (SDM), which can be deployed with multicore (MCF), multimode (MMF), or multiparallel (MPF) fibers, and band division multiplexing (BDM), which involves using a broader spectrum of optical fibers to enable low-loss transmission (e.g., 54 THz in ITU G.652.D fibers). However, SDM solutions such as MCF and MMF can improve transmission capacity but require a complete transformation of the optical transport ecosystem, including new fibers and

devices. On the other hand, BDM, which does not require the deployment of extra optical fibers, is the most feasible immediate option to increase the capacity of the optical network. Although optical amplification is the main issue with the BDM system, there are already several widely available prototype amplifiers that work in the extended spectrum region [3].

Transparent wavelength routing in BDM also needs filtering and switching components to be available. The first move toward putting the BDM approach into practice is the introduction of filtering and switching components. The network component such as a wavelength selective switch (WSS) is vital because it offers autonomous management and routing of each input channel to a fiber output of the WDM comb. WSS systems are generally constructed using complex and bulky technologies like liquid crystal on silicon (LCoS) and microelectromechanical systems (MEMS) [4].

The current study suggests a multi-band WSS implementation utilizing photonic integrated circuit (PIC) technology. This approach contrasts existing bulky WSS systems based on MEMS and LCoS technologies. The proposed WSS has a modular design that can operate in a broad optical spectrum, including the C + L + S-bands. It offers scalability to accommodate additional output fibers and channels with a smaller footprint than traditional MEMS-based solutions. The analysis only focuses on the switching functionality of the WSS module without considering the local add/drop module of the reconfigurable optical add–drop multiplexer (ROADM), as shown in Fig. 1. A preliminary network performance analysis of the proposed multi-band modular WSS is performed by operating it on a symbol rate of $R_s = 60$ GBaud and free spectral range (FSR) = 100 GHz WDM comb to enable 400G transmission [5]. This study begins by proposing the redesign of the WSS to support 800G transmission with FSR = 150 GHz and $R_s = 120$ GBaud and then evaluate its detailed performance considering two different topologies: Italian and German networks. Furthermore, the performance comparison of transparent and translucent networks is also presented for different network configurations. Finally, a detailed comparison has also been made in terms of traffic and channel allocation for multi-band transmission with respect to widely deployed single-band transmission systems.

The remainder of the paper is organized as follows. In Section 2, the proposed architecture of the WSS is described. In Section 3, the WDM transport layer details are briefly described, and the optical signal-to-noise ratio (OSNR) penalty of the proposed WSS is discussed for different symbol rates. Next, in Section 4, the network layer details are reported along with a broad description of the tool used for the network performance analysis. Section 5 describes the network performance results considering different transceivers, transparent and translucent networks, and the SDM versus BDM network configuration comparison. Finally, the conclusion of the paper is stated in Section 6.

2. WAVELENGTH SELECTIVE SWITCH ARCHITECTURE

The ROADM under analysis is based on a photonic integrated WSS, enabling dense wavelength division multiplexing (DWDM) over a multi-band scenario. The underlying design principles of the PIC have been chosen to allow modularity and scalability of the structure, allowing the architecture to be adapted and simulated for various applications, envisioning different amounts of ports, channels, and spectral characteristics. This is achieved through a "divide and conquer" approach, splitting the demultiplexing and switching operations into separate sections while implementing the required functionalities through cascades of simpler integrated components.

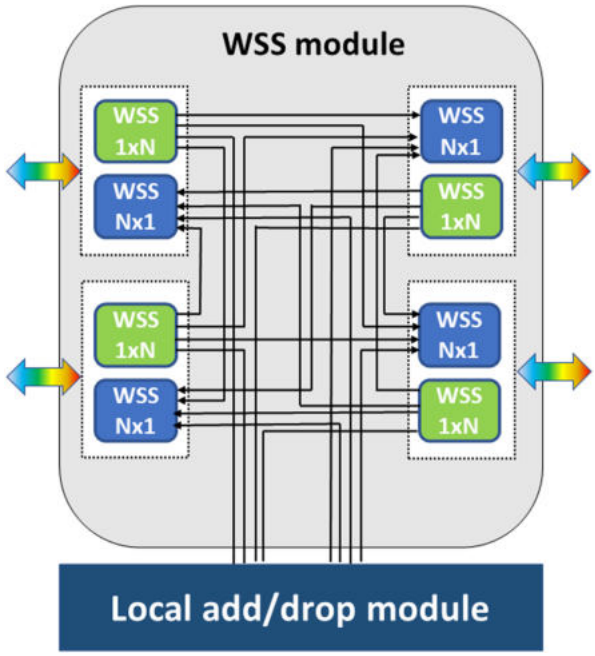

Fig. 1. ROADM architecture enabled by multiple WSS modules.

The main results and the responses of the components are highlighted for a target application in the S + C + L-bands, with channel spacing of FSR = 100 GHz: the following network analysis also considers a case with FSR = 150 GHz, although the same design principles and simulation steps are upheld. The device architecture is depicted in Fig. 2, which highlights both the general structure, the filtering cascade, and the switching network structures [6]. The response of the components has been simulated by analytical means or circuit block-based solutions, using the Synopsys Optsim simulation platform to evaluate the overall WSS performance.

A. Filtering Section

This first section is tasked with demultiplexing the input signal into its channels, separating each into a separate waveguide while introducing minimal losses and cross talk effects. This operation is achieved through a multistage cascaded filtering structure, which starts by separating the main bands of operations (S + C + L in the scenario under analysis) before moving to a finer filtering resolution; this stage is fundamental in both limiting the losses by reducing the following filtering cascade, as well as reducing the inter-band cross talk, allowing the optimized design of the following components for the required band of operation. After this initial division, each spectral sub-region is demultiplexed by a filtering element cascade. Two

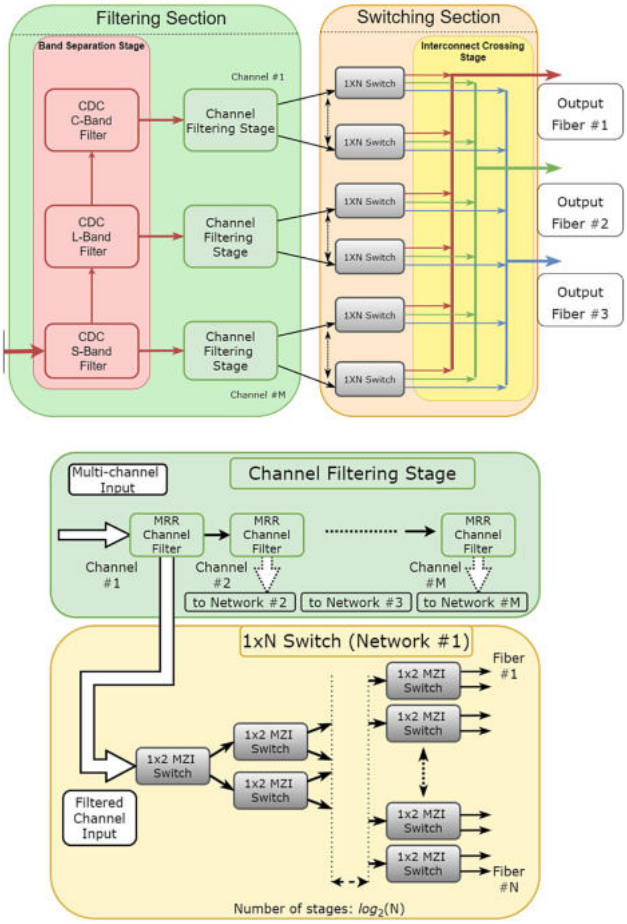

Fig. 2. Circuit model of the proposed WSS structure, highlighting the main operational stages and their block structure.

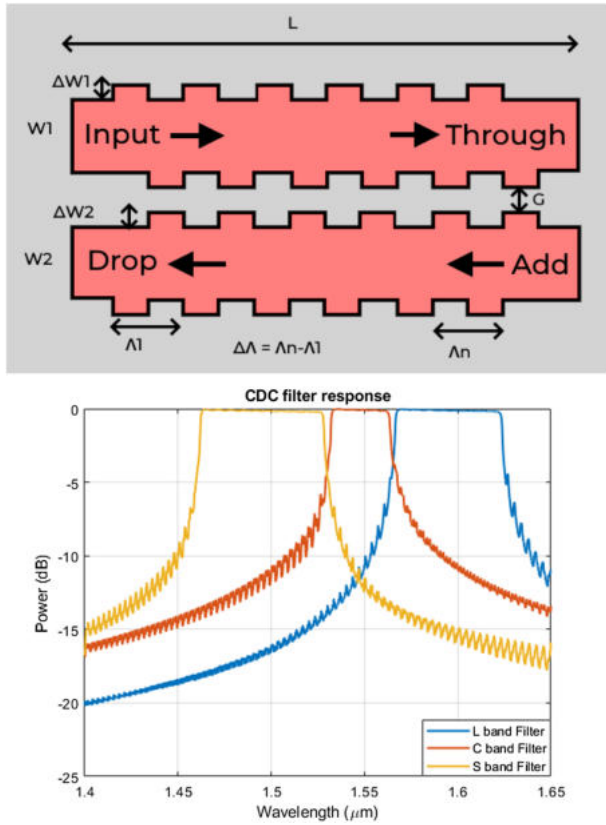

Fig. 3. Contra-directional coupler filter: (top) schematic and (bottom) frequency response.

main devices accomplish this operation: contra-directional couplers (CDCs) for the band separation and micro-ring resonator (MRR)-based filters for the channel demux.

These two elements achieve their wavelength filtering capabilities through different operating principles and are, therefore, suited for different tasks. The operating principle of CDCs is based on the engineering of their gratings, which allows coupling of the forward propagating mode of the first waveguide to the backward propagating mode of the second waveguide. Their main design parameters, highlighted in Fig. 3, are the waveguides and grating geometry: by tuning the waveguide unperturbed effective index (through width $W_{1,2}$ and height) and the perturbed one ($\Delta W_{1,2}$) together with the gap G, we can suppress direct coupling and maximize the contra-directional effect. Through proper engineering of the grating periodicity ($\Lambda_{1,n}$), we can tune the effect for certain bandwidths and central frequencies.

MRRs work instead on a simpler interference principle: during the round trip in the ring structure, only certain frequencies will experience constructive interference, and as such this element can couple selective wavelengths to a second waveguide while leaving the rest of the band unchanged. Single-ring structures have unsatisfactory properties with respect to transmitted spectra flatness and stop band attenuation, although the combination of them in more complex structures can compensate for these effects, as shown in Fig. 4. The design of these structures is mainly affected by two groups of parameters, namely, the coupling coefficients between the elements ($K_{11,12,21,22}$) and the radius of the rings R: by tuning the radii, we can select the target channel, while the coupling coefficients are responsible for the shape of the overall frequency response.

Due to their different operating principle, CDCs and MRRs are suitable for slightly different applications. The CDC structures are ideal for separating the central region of operation due to their flattop wideband properties and sharp stop band transitions: even though they require a larger footprint with respect to other filtering solutions, they can be tailored to cover an ultra wideband of operation [7], making them fundamental building blocks for multi-band applications. On the other hand, MRRs, which are used for channel separation, represent one of the standard integrated solutions for add–drop filtering systems, although they are more suited to channel filtering and cannot achieve ultra-wide filtering bandwidths.

In the proposed architecture, each channel is filtered by a two-stage ladder MRR filter [8]: this configuration allows a flattop response, with a sharp stop band transition and high extinction ratio, ideal for minimizing the inter-channel cross talk and reducing the transmission penalties. To mitigate the issue of aliasing of MRR-based solutions, the devices have been designed and simulated considering more complex grating-assisted coupling structures [9]: these couplers allow for the reduction of the number of filtering elements needed, as additional antialiasing elements are not required unlike in

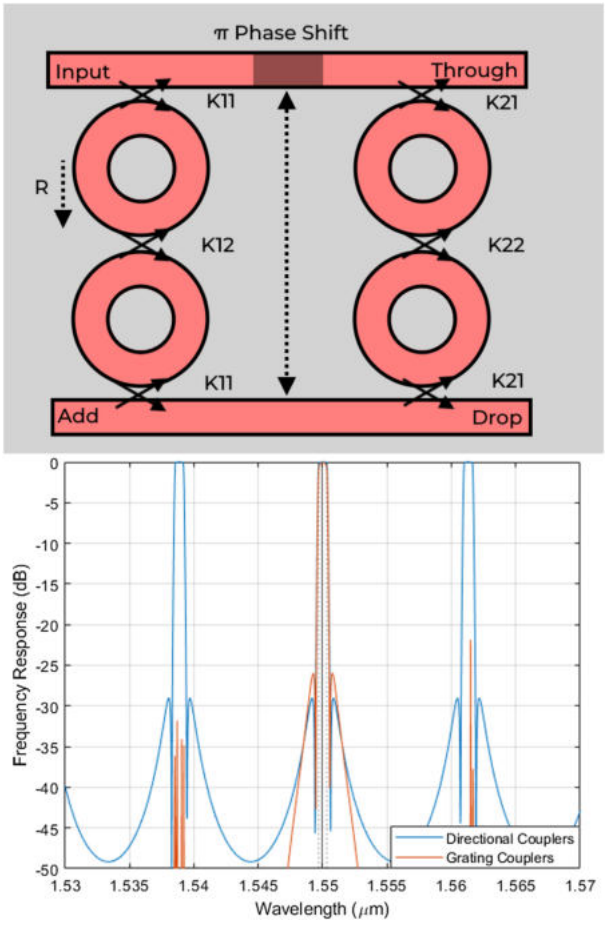

Fig. 4. Device schematic for the two-stage ladder MRR filter. The frequency response is shown for the individual device together with the proposed antialiasing solution.

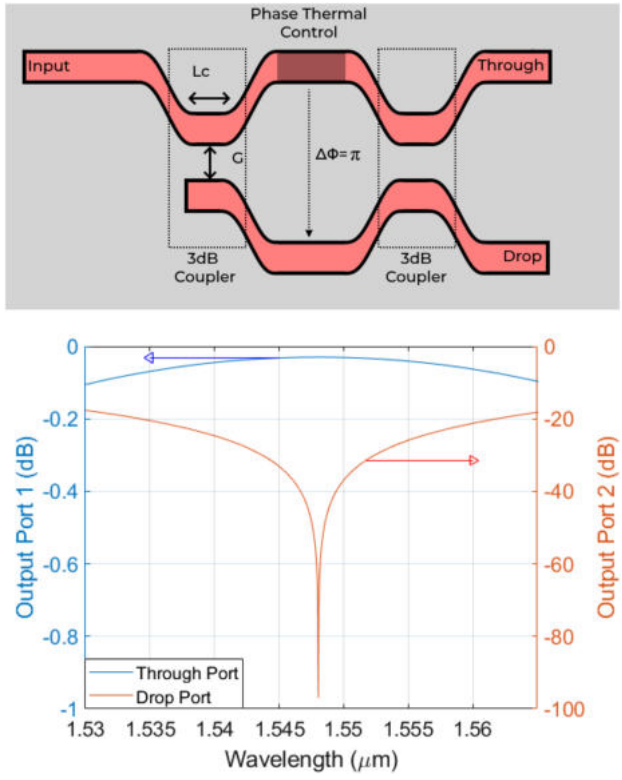

Fig. 5. 1 × 2 Mach–Zehnder interferometer switch: (top) schematic and (bottom) frequency response.

previously reported implementations [5]. This change allows more precise wavelength-dependent engineering of the coupling value, which can compensate for the intrinsic period nature of the response of MRR based device: as depicted in the device frequency response, an FSR-free element can be engineered, which does not introduce channel aliasing. After the demux operation, the following section is specific for routing the signals toward the target output port.

B. Switching Section

In order to completely avoid contention, the routing is achieved through parallel independent switching networks, with each handling an individual channel and propagating it to the target egress port.

These networks are implemented as $1 \times N$ binary tree switches, comprising $N-1$ 1×2 optical switching elements (OSEs), as depicted in the general architecture (Fig. 2). This solution has been chosen instead of a more traditional $M \times N$ crossbar switch as it maintains the same connectivity and routing capabilities while reducing the number of elements and allowing for a more flexible design. While in traditional crossbar structures, the switches must be compatible with all input signals, using parallel independent switching networks, each sub-module can be optimally designed for the expected frequency of operation.

The OSE has been modeled as a Mach–Zehnder interferometer (MZI) switch, as shown in Fig. 5. MZIs are a standard integrated solution for thermal and MEMS-controlled switching structures, as they can be easily implemented and provide a relatively flat wide frequency response, ideal for frequency-independent switching [10–12]. The design of the MZI is relatively straightforward, with the coupling length L_c and the gap G chosen to create 3 dB coupling regions for the wavelength of interest, while thermal control allows the introduction of a π phase shift, which changes the output from the through to the drop port. In our simulation, we envisioned a thermal control strategy, but the use of alternative control schemes does not lead to significant functionality differences.

The active routing section terminates with the switches. The last part of the structure comprises passive waveguide crossings and wavelength combiners to bring all the connections to the target output port, as depicted in Fig. 6. These structures have been modeled as passive lossy elements, considering reference values from the literature for experimental and state-of-the-art devices for crossings [13–15] and integrated wavelength combiners [16,17].

3. WDM TRANSPORT LAYER

Having defined all the relevant components and the general architecture, to assess the proposed architecture's network effect, the transmission impairments and effects must be evaluated in a digital signal processing (DSP)-aware simulation

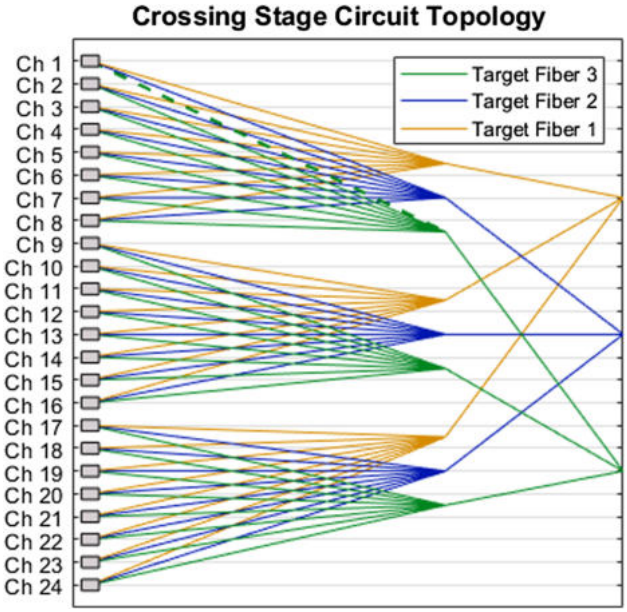

Fig. 6. Interconnect stage topology for a 24 channel device with 3 target output ports.

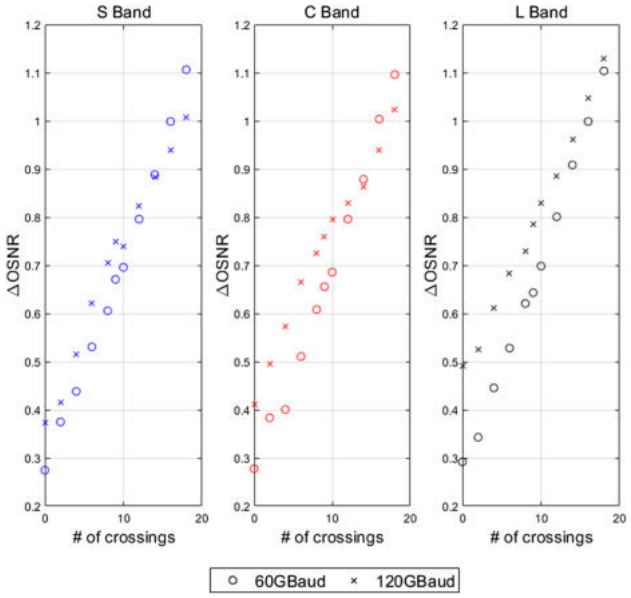

Fig. 7. ΔOSNR penalty distribution for a tested channel comparing the 60 Gbaud and the 120 GBaud performance.

platform, allowing the characterization of the component. With respect to standard frequency response evaluation, which only addresses the insertion loss and qualitative shaping of a broadband signal, this simulation process is able to extract the impairment of the device by considering symbol transmission under a defined modulation format and telecom scenario: this method can characterize the bit-error rate or symbol-error rate introduced by the device under test.

Two main coherent transmission scenarios are considered, using a 16QAM modulation format with a symbol rate of $R_s = 60$ GBaud over a FSR = 100 GHz WDM comb for the first case and $R_s = 120$ GBaud over a FSR = 150 GHz WDM comb for the second one. The relevant components (filters and switching elements) have been designed for the two applications following the same principles to minimize the cross talk and penalties. The device is then simulated in the Optsim Photonic Circuit Simulation Suite: while the transmitter and receiver modules are implemented through the Suite library, each circuit component has been implemented based on the frequency response extracted from the device simulations, using a wide range of techniques, from the beam propagation method (BPM), finite-difference time-domain (FDTD), coupled mode theory (CMT), and analytical models. The OSNR penalty (ΔOSNR) has been chosen as the QoT metric, evaluated for a target bit-error rate (BER) $= 10^{-3}$. For the proposed structure, two main contributions of the penalty can be highlighted: the path-dependent penalty, due to the crossing interconnect stage, and the path-independent effects, due to the fixed filtering and switching elements. For our analysis, the response of the components has been otherwise normalized apart from the two effects, focusing on the QoT impairment and assuming the ideal recovery of the insertion losses.

The DSP simulations are executed for a 24 channel 1×3 WSS, extracting the ΔOSNR for all possible routing configurations in both the 60 GBaud and 120 GBaud case. The path-dependent or routing penalty can be highlighted by displaying the data as a function of the number of waveguide crossings encountered, as shown in Fig. 7. The average penalties are depicted for both cases and show compatible results for the two transmission scenarios: the fluctuations are justified by the probabilistic nature of the BER simulations, which can lead to slight discrepancies in the average value due to spurious results. Based on these simulation results, a general prediction model can be built to arbitrarily increase the cardinality of the WSS, i.e., the number of input channels and output fibers, relying on the path-dependent penalty estimation and the extrapolation of the data linearity. By evaluating the crossing topology for a target M channel $1 \times N$ WSS and adjusting for the cascading effects of the components, the penalty can be predicted for any routing configuration, allowing larger-scale simulations based on a reduced data set. This expansion of the original simulation data accounts for both the filtering penalties introduced by the WSS device, which are based on the cascaded effect of the normalized components, while an additional path-dependent loss is considered due to the larger topology of the multiplexing section. The insertion losses of the de-multiplexing and switching stage are considered compensated due to their fixed nature, which is not affected by the routing configuration of the device.

The topology-based expansion of the model is necessary due to the computational cost of the DSP-enabled simulations: as the device scales up, this analysis becomes prohibitive in both required resources and computational time, as such the mathematical extrapolation of the data poses a good trade-off, using the smaller footprint results to estimate the device behavior. At the same time, some form of synthetic penalty estimation would still be required at the system level. For large-footprint circuits, the simulation would also require a careful evaluation of the manufacturing uncertainty and topology optimizations, which falls outside the scope of our current investigation.

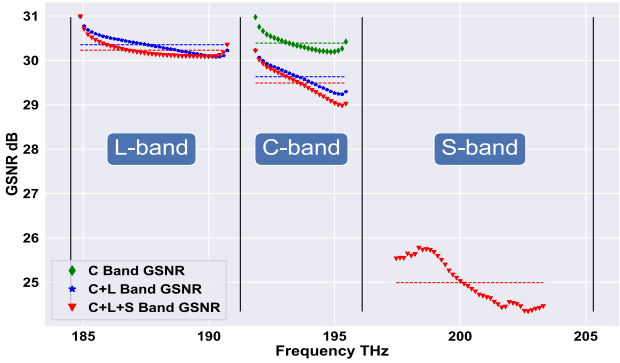

Fig. 8. GSNR versus frequency for 105 channels (S + C + L - 25 + 40 + 40 channels) for all scenarios (C-band only, C + L, and S + C + L).

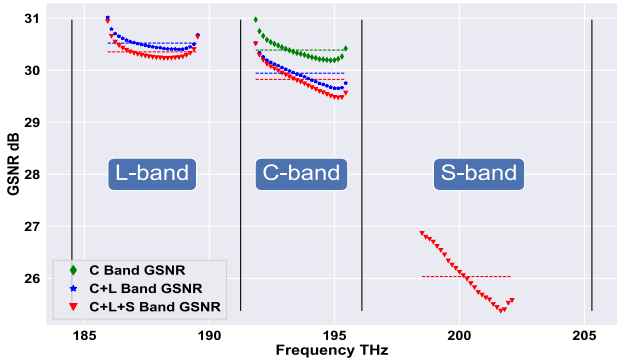

Fig. 9. GSNR versus frequency for 25 channels/band for all scenarios (C-band only, C + L, and S + C + L).

4. NETWORK PERFORMANCE ANALYSIS

The overall performance of the network is examined in order to evaluate the effect of the new WSS architecture on various optical transport solutions. The statistical network assessment process (SNAP) [18] is used for this purpose, which operates at the physical layer of the network being tested and assesses the degradation of QoT caused by each network element. In this study, a disaggregated abstraction of the physical layer is adopted, where each network element is assumed to introduce gain or loss as well as Gaussian disturbance. This includes amplified spontaneous emission (ASE) noise from amplifiers and non-linear interference (NLI) from fiber propagation. As a result, the GSNR for the ith channel under test is defined as

$$\mathrm{GSNR}_i = \frac{P_{\mathrm{S},i}}{P_{\mathrm{ASE}(f_i)} + P_{\mathrm{NLI},i}(f_i)}, \quad \textbf{(1)}$$

where $P_{\mathrm{S},i}$ denotes the signal launch power, and $P_{\mathrm{ASE}(f_i)}$ is the ASE, while $P_{\mathrm{NLI},i}(f_i)$ is the fiber NLI [19,20].

Our analysis assumes that the optical amplifiers in a multi-band optical system, including the C- and L-band channels amplified by commercial erbium-doped fiber amplifiers (EDFAs) and the S-band channels amplified with a thulium-doped fiber amplifier (TDFA), are tuned separately for each band. The amplified lines consist of identical 75 km single-mode fibers that comply with the ITU-T G.652D standard. The transceivers for each frequency operate on the ITU-T 100 GHz WDM grid with $R_s = 60$ GBaud for 400G transceivers [5] and the 150 GHz WDM grid with $R_s = 120$ GBaud for 800G transceivers [21]. The study adopts a span-by-span approach to optimize the input power for the C-, L-, and S-bands, using the local optimization global optimization (LOGO) algorithm to maximize the QoT. The GSNR profile versus frequency of a single span of 75 km for the C-, C + L-, and S + C + L-bands for FSR = 100 GHz is already shown in [5]. In this analysis, we have considered reasonably loaded C-, L-, and S-bands at FSR = 150 GHz, which results in 105 channels [C-band-25 (≈4 THz), L-band-40 (6 THz), and S-band-40 (6 THz) channels] shown in Fig. 8 and also the fully loaded C-band only with a normalized number of channels in other bands [C-band-25 (≈4 THz), L-band-25 (≈4 THz) and S-band-25 (≈4 THz) channels] shown in Fig. 9.

Figure 8 illustrates the GSNR values obtained for almost the entire spectrum of C- and L-bands and partially covering the S-band represented by dotted lines indicating the average. The average GSNR for the C-band only in this case is 30.42 dB, whereas for the C + L-band, the average GSNR obtained for the C-band is 29.7 dB, and for the L-band, the average GSNR is 30.3 dB. When activating all bands (S + C + L), the average GSNR value for the C-band is 29.5 dB, the average GSNR value for the L-band is 30.15 dB, and for the S-band, it is 25 dB. Similarly, Fig. 9 shows the GSNR profile for a window of approximately 4 THz for each band. The average GSNR for the C-band only is 30.4 dB, while for the C + L-band, the average GSNR for the C-band drops to 29.9 dB, and the L-band GSNR average is 30.45 dB. With activation of the three S + C + L-bands, the average GSNR for the C-band decreases to 29.7 dB, the average GSNR of the L-band is 30.2 dB, and the S-band average GSNR is 26 dB. In the C + L- and S + C +-L band scenarios, the average GSNR of the C-band and L-band is lower than the reference C-band transmission case, mainly due to the iterative impact of SRS and NLI.

The routing and wavelength assignment (RWA) algorithm is used to designate light-paths (LPs); specifically, the k-shortest routes with $k = 5$ are used for routing, and the first-fit technique is used to allot spectrum. To reduce the need to establish new LPs, traffic grooming is attempted by verifying the availability of idle capacity in existing LPs. If a new LP needs to be established, the optical controller selects the appropriate modulation format based on the estimated QoT and the required GSNR (RGSNR) for the transceiver [22]. In addition, the network evaluation is conducted with a uniform traffic distribution among all nodes in the network.

In this work, we have considered the German and Italian topologies illustrated in Fig. 10 and Fig. 11, respectively. The German topology comprises 17 optical nodes (red dots) that represent the ROADMs, where traffic request is added/dropped, and 26 edges (blue lines) that represent the optical line systems comprised of fiber pairs and in-line amplifiers, with an average node degree of 3.1, an average inter-node distance of 207 km, and a maximum link length of 300 km. On the other hand, the Italian topology consists of 21 nodes and 36 edges, with an average node degree of 3.43, an average

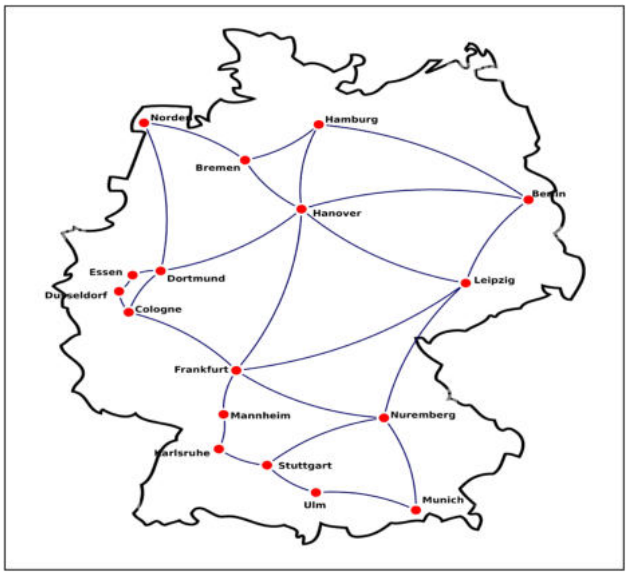

Fig. 10. German topology.

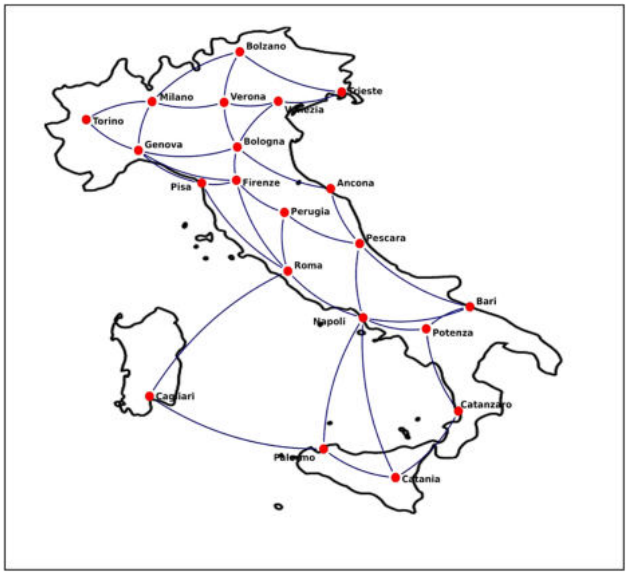

Fig. 11. Italian topology.

inter-node distance of 209 km, and a maximum link length of 400 km.

5. RESULTS AND DISCUSSION

This section shows the results obtained for the two network topologies under consideration. Throughout our analysis, we used the upgraded WSS device described in Section 2, and we evaluated its impact on various networking scenarios, including the multi-band scenario. We commence by comparing the performance of different transceivers, 400G and 800G, followed by assessing the utilization of regenerators and their effect on the overall network performance in terms of traffic allocation. Lastly, to ensure a fair evaluation of multi-band results when implementing the proposed WSS structure in a ROADM architecture, we compare the performance of BDM and SDM networks regarding channel allocation. Blocking probability is a key performance metric in network analysis, particularly in the context of allocation of network resources and capacity planning. It quantifies the probability that a new connection request is denied or "blocked" due to insufficient resources, such as available channels or bandwidth. The blocking probability threshold is set at BP $= 10^{-2}$ for all the analyses and is calculated by dividing the number of blocked connection requests by the total number of connection requests attempted within the network. We assume a core continuity constraint (CCC) in the single-band scenario, which requires that each LP be allocated in the same fiber from the source to the destination node and corresponds to the switching technique [23]. This method is preferred because it yields two or three times as many fiber pairs as the multi-band method in C + L and C + L + S.

A. 400G versus 800G Transceiver

By switching to higher capacity transceivers, it is possible to achieve a lower cost per bit as more modulation levels are available, along with higher baud rates. Our analysis compared the 400G and 800G transceivers while limiting the maximum modulation format to 16QAM to ensure a fair comparison.

The simulations are executed for the German network topology for the multi-band scenario for three transceivers: 400G, 800G, and ideal. The ideal case is the theoretical maximum traffic limit that can be achieved. The results of optimized transmission are utilized to conduct network-level analysis by using the GSNR values for each WDM channel to generate a topological graph. This graph is weighted by GSNR degradation to implement SNAP. In all the cases depicted in Figs. 12–15, SNAP is applied. As a reference, we take the C-band 1× fiber and compare it to the C-band 2× fibers with the C + L multi-band and the C-band 3× fibers with the C + L + S multi-band. We employed different parameters for the 400G and 800G transceiver cases. Specifically, for the 400G transceiver, we utilized a channel spacing of 100 GHz and a baud rate of 60 Gbaud. In the case of the 800G transceiver, we employed a channel spacing of 150 GHz and a baud rate of 120 Gbaud. To maintain consistency, we normalized all frequency bands to ≈4 THz for both the 400G and 800G transceivers, shown in Figs. 12 and 13. For the 800G transceiver, we also evaluated its performance with an extended

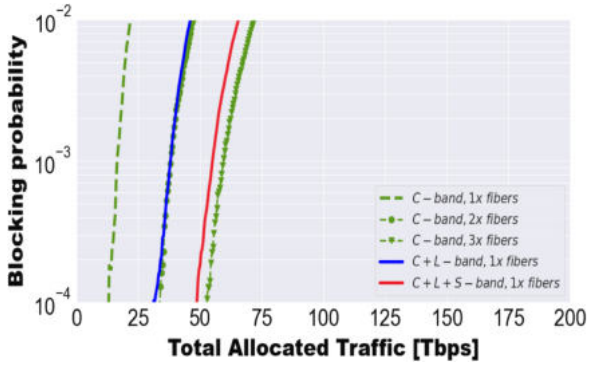

Fig. 12. Blocking probability evaluated over the German network (≈4 THz/band) considering 400G transceivers.

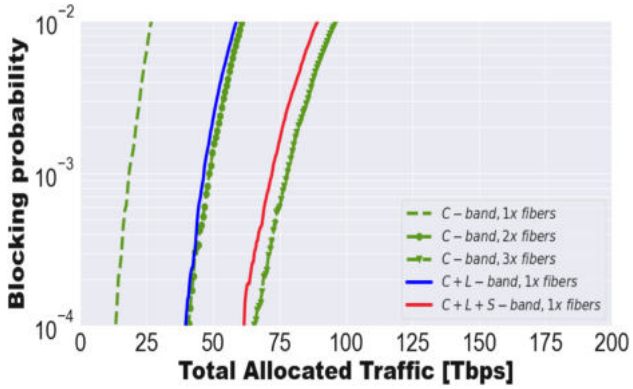

Fig. 13. Blocking probability evaluated over the German network (≈4 THz/band) considering 800G transceivers.

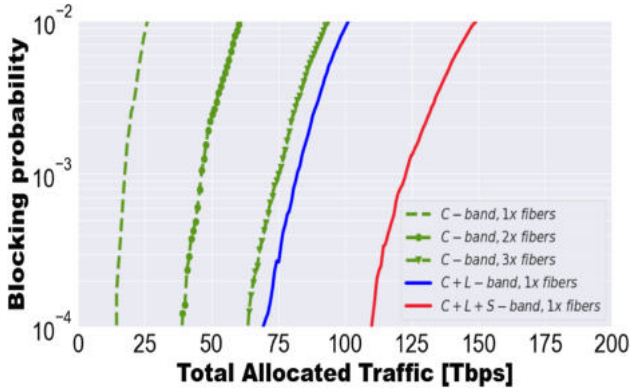

Fig. 14. Blocking probability evaluated over the German network (C/L/S-band ≈4 THz/6 THz/6 THz) considering 800G transceivers.

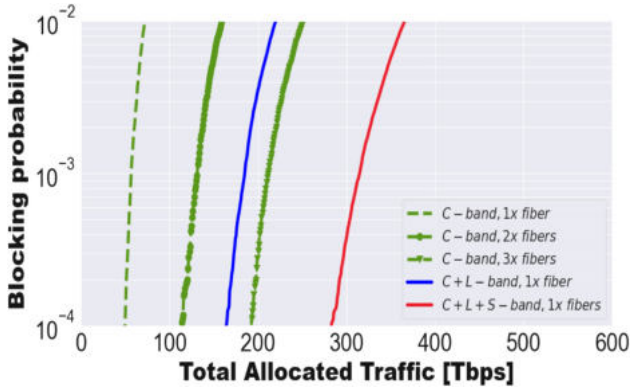

Fig. 15. Blocking probability evaluated over the German network considering ideal transceivers.

bandwidth of up to 6 THz for the L- and S-bands and ≈4 THz for the C-band, shown in Fig. 14.

The plot in Fig. 12 illustrates the traffic allocation versus the blocking probability for the 400G transceiver case. The C-band 1× fiber has a delivery capacity of approximately 23 Tbps. When we consider C-band 2× fibers and multi-band C + L 1× fiber, they perform similarly and can allocate traffic of roughly 45 Tbps. With C-band 3× fiber, we can achieve approximately 73 Tbps; with multi-band C + L + S 1× fiber, we can assign approximately 68 Tbps. The plot in Fig. 13 illustrates the traffic allocation versus the blocking probability for the 800G transceiver case. The C-band 1× fiber has a delivery capacity of approximately 27 Tbps. When we consider C-band 2× fibers and multi-band C + L 1× fiber, they perform similarly and can allocate traffic of roughly 60 Tbps. With C-band 3× fiber, we can achieve approximately 92 Tbps; with multi-band C + L + S 1× fiber, we can assign approximately 87 Tbps. In the latter scenario of both the 400G and 800G having almost the same bandwidth, the traffic allocation is slightly higher in the 3× fiber than in the multi-band scenario. This is due to the introduction of a non-linear propagation penalty when transmitting three bands (C + L + S) on a single fiber.

The plot in the Fig. 14 illustrates the traffic allocation versus blocking probability for the 800G transceiver case for the extended L- and S-bands (≈6 THz spectrum usage). The delivery capacity of the reference C-band 1× fiber is approximately 28 Tbps. For the C-band 2× fiber, the traffic allocation is nearly 55 Tbps, whereas, for the multi-band C + L 1× fiber case, the traffic allocation is slightly greater than 100 Tbps. The difference in traffic allocation is more significant in the multi-band case due to the greater spectrum usage in the C + L-bands, with almost 10 THz of spectrum usage compared to the 7.5 THz in the C-band 2× fiber. With C-band 3× fiber, we can achieve approximately 94 Tbps, and with multi-band C + L + S 1× fiber, we can allocate around 148 Tbps, mainly due to the higher spectrum usage in the latter case, which is approximately 15 THz. The C + L + S-band for the 400G transceiver has a capacity of 5.67 b/Hz, while the 800G transceiver has a C + L + S-band capacity of 14.6 b/Hz. Overall, the 800G transceiver provides better traffic allocation than the 400G transceiver, with a significant difference in the multi-band C + L + S scenario due to the higher spectrum usage.

The Fig. 15 represents the ideal transceiver scenario with zero penalties, representing the maximum achievable traffic capacity, and is higher than the capacity achievable with the 800G transceiver. According to the graphs, the C-band reference has a maximum attainable traffic allocation of around 75 Tbps. In comparison, the C-band 2× fiber and C-band 3× fiber have achievable capacities of 150 Tbps and 250 Tbps, respectively. The attainable capacity is around 215 Tbps for the multi-band C + L scenario, and it is slightly greater than

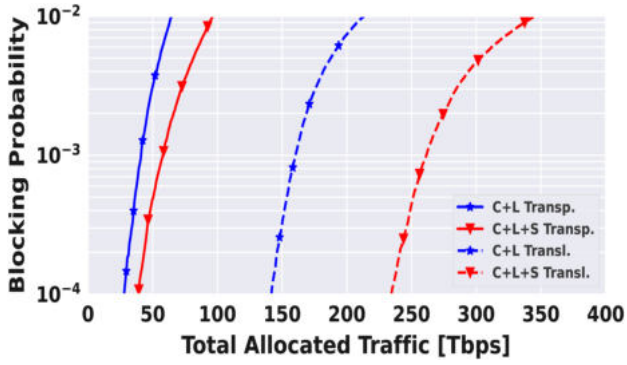

Fig. 16. Network capacity for transparent and translucent network design for the C-, C + L-, and S + C + L-band with 800 Gb/s traffic request size in the Italian network topology.

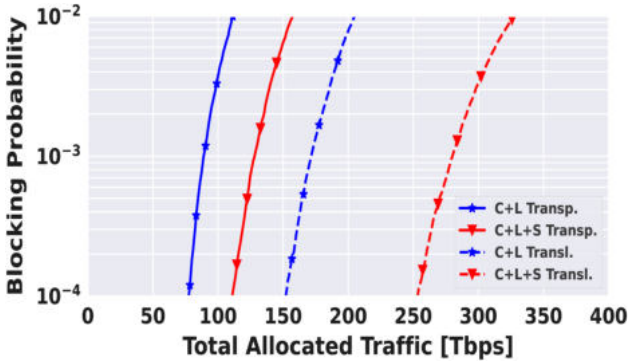

Fig. 17. Network capacity for transparent and translucent network design for the C-, C + L-, and C + L + S-band with 800 Gb/s traffic request size in the German network topology.

350 Tbps for the multi-band C + L + S scenario. When comparing these ideal transceiver scenarios, it can be observed that the 800G transceiver can still effectively distribute traffic despite penalties. Additionally, in the comparison between the 400G and 800G transceivers, the 800G model demonstrates better traffic allocation and a higher bits per Hertz ratio.

B. Transparent versus Translucent

In the context of a transparent network, our approach involves establishing a new LP that spans end-to-end, utilizing the highest achievable modulation format without intermediate regeneration and adhering to the wavelength continuity constraint across all links in the path. However, in translucent scenarios, this constraint is eliminated at nodes where regeneration occurs, which involves using a pair of back-to-back transceivers. To ensure that the maximum bit rate of 800 Gbps

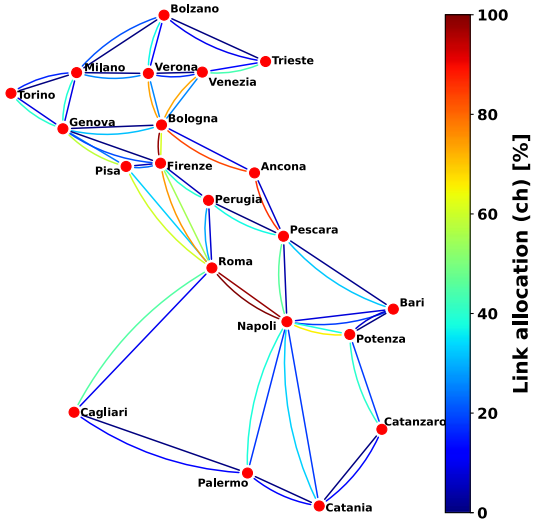

(a) SDM (C-band - 50 channels, 2x fibers)

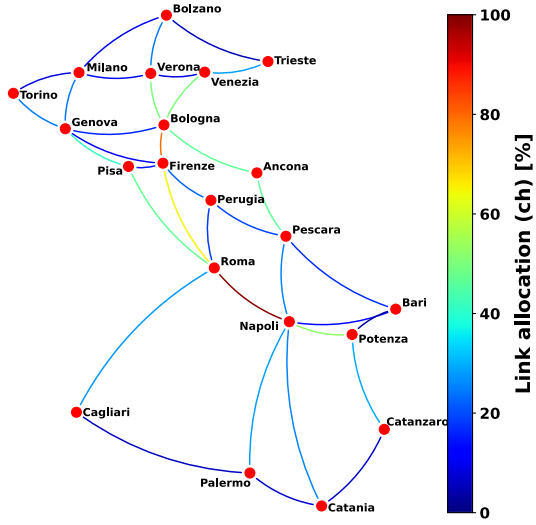

(b) BDM (C+L-band - 50 channels, 1x fiber)

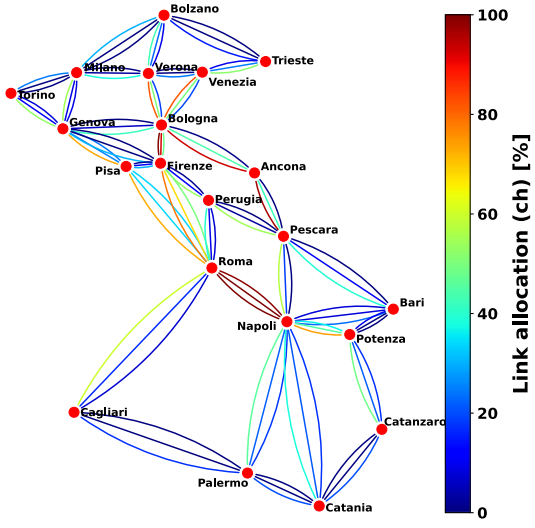

(c) SDM (C-band - 75 channels, 3x fibers)

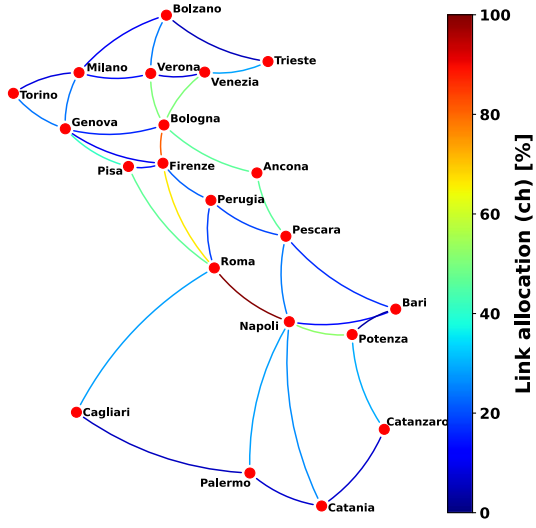

(d) BDM (C+L+S-band - 75 channels, 1x fibers)

Fig. 18. Italian topology channel allocation comparison—800G transceiver.

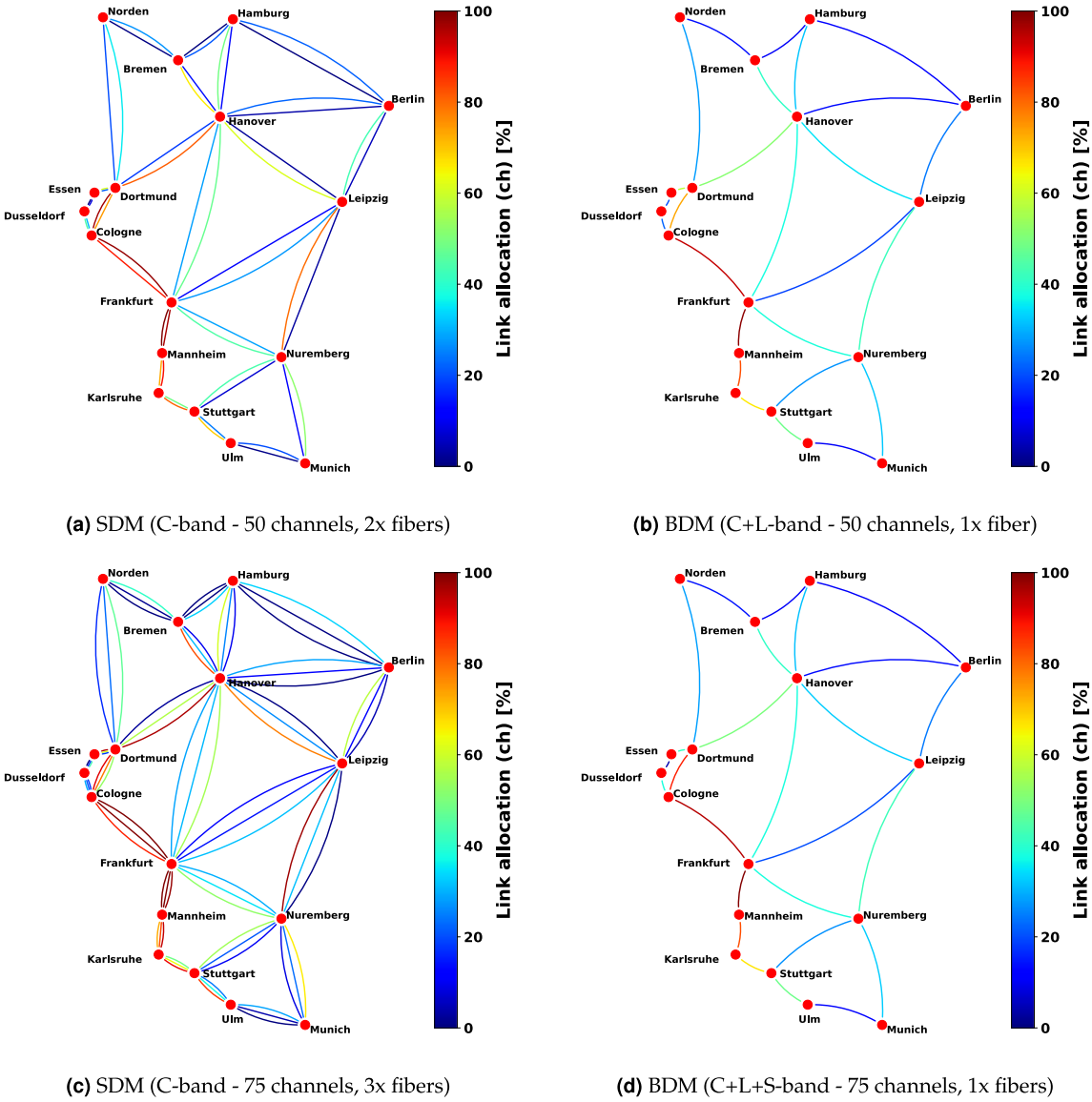

(a) SDM (C-band - 50 channels, 2x fibers)

(b) BDM (C+L-band - 50 channels, 1x fiber)

(c) SDM (C-band - 75 channels, 3x fibers)

(d) BDM (C+L+S-band - 75 channels, 1x fibers)

Fig. 19. German topology channel allocation comparison—800G transceiver.

(16QAM) is maintained for the LP, our controller activates an additional pair of transceivers at intermediate nodes when necessary.

The results are obtained for the multi-band (C + L- and C + L + S-bands) scenario for both the Italian and German networks shown in Fig. 16 and Fig. 17, respectively. The Italian network has slightly greater link lengths than the German network. In Fig. 16, it can be observed that in the transparent scenario, the total traffic allocated for the C + L-band is 65 Tbps, whereas, for the translucent scheme, it is 220 Tbps. Similarly, for the C + L + S-band, the allocated traffic is almost 100 Tbps in the transparent scenario, while it is around 350 Tbps in the translucent scenario. Likewise, the data presented for the German network in Fig. 17 reveals that in the transparent scenario, the total traffic assigned to the C + L-band amounts to 120 Tbps, whereas in the translucent setup, it rises to 210 Tbps. Additionally, in the case of the C + L + S-band, the allocated traffic is approximately 155 Tbps in the transparent scenario, whereas it reaches around 330 Tbps in the translucent design.

The higher traffic allocation in the translucent scenario compared to the transparent procedure is due to removing the wavelength continuity constraint at the intermediate nodes where regeneration is performed. This allows for more flexibility in traffic routing and enables the use of additional wavelengths, leading to higher traffic capacity. Additionally, activating extra pairs of transceivers on intermediate nodes when necessary to maintain the maximum bit rate for that LP (800 Gbps) also contributes to the higher traffic allocation in the translucent scenario.

C. SDM versus BDM Comparison in Terms of Channels

To ensure a fair comparison, we evaluated multi-band results using the proposed WSS structure integrated into

Table 1. SDM versus BDM Link Allocation Details

	Link Allocation (Channel) %			
Topology	C-band, 2× fibers	C + L-band	C-band, 3× fibers	C + L + S-band
Italian	28.17	27.95	29.38	28.16
German	39.62	38.83	40.2	39.58

the ROADM architecture to assess the performance of BDM and SDM networks [24]. While the BDM method used multi-bands (C + L and C + L + S), our study used the SNAP network performance analysis, presuming SDM with numerous fibers in the C-band on the same total spectrum. We took into account different fibers (2× and 3×) for SDM and maintained the L- and S-band channel limit at 25 while utilizing almost 4 THz of spectrum per band to effectively compare the link capabilities.

The evaluation is carried out on both the network topologies (Italian and German) by considering the allocation of channels (25 channels per band) in both scenarios of SDM with multiple fibers and BDM for 800G transceiver. The comparison between SDM (2× fibers, 50 channels) and BDM (C + L, 50 channels per fiber) is depicted in Figs. 18(a) and 18(b), while Figs. 18(c) and 18(d) illustrate the comparison between SDM (3× fibers, 75 channels) and BDM (C + L + S, 75 channels per fiber) for the Italian topology. Likewise, the comparison between SDM (2× fibers, 50 channels) and BDM (C + L, 50 channels per fiber) is depicted in Figs. 19(a) and 19(b), while Figs. 19(c) and 19(d) illustrate the comparison between SDM (3× fibers, 75 channels) and BDM (C + L + S, 75 channels per fiber) for the German topology. The allocation of links based on channel utilization is visualized as a heat map, where a darker shade of orange indicates a higher percentage of channel allocation, while blue represents a lower percentage of channel allocation.

The link allocation in terms of channel for the SDM and BDM scenarios for both network topologies is shown in Table 1. The multi-band BDM scenario has slightly lower channel allocation in both network scenarios than the single-band SDM scenario. However, the difference between SDM and BDM increases slightly in the case of SDM with three fibers and multi-band BDM (S + C + L-bands) due to nonlinear propagation caused by transmitting all three bands on a single fiber.

6. CONCLUSION

This work proposed a networking performance evaluation for a modular photonic integrated wideband WSS that supports multi-band operation across different spectral regions. Our proposed multi-band WSS serves as a switching section of a ROADM architecture, and we analyzed the performance of different transceivers and the impact of regenerators on network performance. Our findings reveal that higher capacity transceivers result in improved traffic allocation when considering the same bandwidth, and specifically, the 800G transceiver outperforms the 400G transceiver in terms of traffic allocation. Additionally, we have shown the impact of regenerators on the network using the 800G transceiver and the proposed multi-band WSS on the network traffic allocations. We also conducted a fair evaluation of multi-band (C + L- and C + L + S-bands) results with the widely deployed C-band and its impact on the channel allocation, keeping the same number of channels for each band. Our study provides valuable insights into optimal network configurations that maximize network capacity and performance.

Funding. H2020 Marie Skłodowska-Curie Actions (814276).

Acknowledgment. Portions of this work were presented at the GLOBECOM 2022 conference in a work with the title "Network performance of ROADM architecture enabled by novel wideband-integrated WSS." The presented work has been supported by the EU within the Italian National Recovery and Resilience Plan (NRRP) of NextGenerationEU, partnership on "Telecommunications of the Future." This project has received funding from the European Union's Horizon 2020 research and innovation program under the Marie Skłodowska-Curie grant agreement 814276.

REFERENCES

1. "Cisco Annual Internet Report 2018–2023," 2020, https://www.cisco.com/c/en/us/solutions/collateral/executive-perspectives/annual-internet-report/white-paper-c11-741490.html.
2. A. Ferrari, A. Napoli, J. K. Fischer, N. Costa, A. D'Amico, J. Pedro, W. Forysiak, E. Pincemin, A. Lord, A. Stavdas, J. P. F.-P. Gimenez, G. Roelkens, N. Calabretta, S. Abrate, B. Sommerkorn-Krombholz, and V. Curri, "Assessment on the achievable throughput of multi-band ITU-T G.652.D fiber transmission systems," J. Lightwave Technol. **38**, 4279–4291 (2020).
3. V. Curri, "Multiband optical transport: a cost-effective and seamless increase of network capacity," in *Photonic Networks and Devices (PND)* (Optica Publishing Group, 2021), paper NeTu2C.3.
4. T. A. Strasser and J. L. Wagener, "Wavelength-selective switches for ROADM applications," IEEE J. Sel. Top. Quantum Electron. **16**, 1150–1157 (2010).
5. M. U. Masood, I. Khan, L. Tunesi, B. Correia, E. Ghillino, P. Bardella, A. Carena, and V. Curri, "Network performance of ROADM architecture enabled by novel wideband-integrated WSS," in *IEEE Global Communications Conference (GLOBECOM)* (2022), pp. 2945–2950.
6. L. Tunesi, I. Khan, M. U. Masood, E. Ghillino, A. Carena, V. Curri, and P. Bardella, "Modular photonic-integrated device for multi-band wavelength-selective switching," in *27th OptoElectronics and Communications Conference (OECC) and International Conference on Photonics in Switching and Computing (PSC)* (2022).
7. M. Hammood, A. Mistry, H. Yun, M. Ma, S. Lin, L. Chrostowski, and N. A. F. Jaeger, "Broadband, silicon photonic, optical add–drop filters with 3 dB bandwidths up to 11 THz," Opt. Lett. **46**, 2738–2741 (2021).
8. A. P. Masilamani and V. Van, "Design and realization of a two-stage microring ladder filter in silicon-on-insulator," Opt. Express **20**, 24708–24713 (2012).
9. N. Eid, R. Boeck, H. Jayatilleka, L. Chrostowski, W. Shi, and N. A. F. Jaeger, "FSR-free silicon-on-insulator microring resonator based filter with bent contra-directional couplers," Opt. Express **24**, 29009–29021 (2016).
10. X. Tu, C. Song, T. Huang, Z. Chen, and H. Fu, "State of the art and perspectives on silicon photonic switches," Micromachines **10**, 51 (2019).
11. N. Dupuis, A. V. Rylyakov, C. L. Schow, D. M. Kuchta, C. W. Baks, J. S. Orcutt, D. M. Gill, W. M. J. Green, and B. G. Lee, "Ultralow crosstalk nanosecond-scale nested 2 × 2 Mach–Zehnder silicon photonic switch," Opt. Lett. **41**, 3002–3005 (2016).
12. Z. Lu, D. Celo, H. Mehrvar, E. Bernier, and L. Chrostowski, "High-performance silicon photonic tri-state switch based on balanced nested Mach-Zehnder interferometer," Sci. Rep. **7**, 12244 (2017).
13. D. Yi, W. Zhou, Y. Zhang, and H. K. Tsang, "Inverse design of multi-band and wideband waveguide crossings," Opt. Lett. **46**, 884–887 (2021).

14. Z. Yu, A. Feng, X. Xi, and X. Sun, "Inverse-designed low-loss and wideband polarization-insensitive silicon waveguide crossing," Opt. Lett. **44**, 77–80 (2019).
15. S. Wu, X. Mu, L. Cheng, S. Mao, and H. Fu, "State-of-the-art and perspectives on silicon waveguide crossings: a review," Micromachines **11**, 326 (2020).
16. S. Singh, K. Kojima, T. Koike-Akino, B. Wang, K. Parsons, S. Nishikawa, and E. Yagyu, "An MMI-based wavelength combiner employing non-uniform refractive index distribution," Opt. Express **22**, 8533–8540 (2014).
17. J. Mu, S. A. Vázquez-Córdova, M. A. Sefunc, Y.-S. Yong, and S. M. García-Blanco, "A low-loss and broadband MMI-based multi/demultiplexer in Si_3N_4/SiO_2 technology," J. Lightwave Technol. **34**, 3603–3609 (2016).
18. V. Curri, M. Cantono, and R. Gaudino, "Elastic all-optical networks: a new paradigm enabled by the physical layer. How to optimize network performances?" J. Lightwave Technol. **35**, 1211–1221 (2017).
19. A. Carena, V. Curri, G. Bosco, P. Poggiolini, and F. Forghieri, "Modeling of the impact of nonlinear propagation effects in uncompensated optical coherent transmission links," J. Lightwave Technol. **30**, 1524–1539 (2012).
20. M. Cantono, D. Pilori, A. Ferrari, C. Catanese, J. Thouras, J.-L. Augé, and V. Curri, "On the interplay of nonlinear interference generation with stimulated Raman scattering for QoT estimation," J. Lightwave Technol. **36**, 3131–3141 (2018).
21. Q. Zheng, H. Yang, L. Wang, Z. Xiao, and H. Zhang, "Single-carrier 800 Gbit/s and 1.2 Tbit/s transmission using 96 GBaud commercial optoelectronic components," in *Asia Communications and Photonics Conference* (Optica Publishing Group, 2021), paper T1B.4.
22. R. Sadeghi, B. Correia, E. Virgillito, A. Napoli, N. Costa, J. Pedro, and V. Curri, "Performance comparison of translucent C-band and transparent C+L-band network," in *Optical Fiber Communication Conference* (Optica Publishing Group, 2021), paper M3E.4.
23. P. S. Khodashenas, J. M. Rivas-Moscoso, D. Siracusa, F. Pederzolli, B. Shariati, D. Klonidis, E. Salvadori, and I. Tomkos, "Comparison of spectral and spatial super-channel allocation schemes for SDM networks," J. Lightwave Technol. **34**, 2710–2716 (2016).
24. M. U. Masood, I. Khan, L. Tunesi, B. Correia, R. Sadeghi, E. Ghillino, P. Bardella, A. Carena, and V. Curri, "Networking analysis of photonics integrated multiband WSS based ROADM architecture," in *International Conference on Software, Telecommunications and Computer Networks (SoftCOM)* (IEEE, 2022).